Elastic and Thermodynamic Properties of Complex Mg-Al Intermetallic Compounds via Orbital-Free Density Functional Theory

Houlong Zhuang, Mohan Chen, and Emily A. Carter

Phys. Rev. Applied **5**, 064021 — Published 30 June 2016

DOI: 10.1103/PhysRevApplied.5.064021

Elastic and thermodynamic properties of complex Mg-Al intermetallic compounds via orbital-free density functional theory

Houlong Zhuang,[1] Mohan Chen,[1] and Emily A. Carter[1,2,*]

[1] Department of Mechanical and Aerospace Engineering, Princeton University, Princeton, NJ 08544, USA
[2] Program in Applied and Computational Mathematics, and Andlinger Center for Energy and the Environment, Princeton University, Princeton, NJ 08544, USA
*eac@princeton.edu

Abstract

Magnesium-Aluminum (Mg-Al) alloys are important metal alloys with a wide range of engineering applications. We investigate the elastic and thermodynamic properties of Mg, Al, and four stoichiometric Mg-Al compounds including $Mg_{17}Al_{12}$, $Mg_{13}Al_{14}$, and $Mg_{23}Al_{30}$, and $MgAl_2$ with orbital-free density functional theory (OFDFT). We first calculate the lattice constants, zero-temperature formation energy, and independent elastic constants of these six materials and compare the results to those computed via Kohn-Sham DFT (KSDFT) benchmarks. We obtain excellent agreement between these two methods. Our calculated elastic constants of hexagonal close-packed Mg and face-centered cubic Al are also consistent with available experimental data. We next compute their phonon spectra using the force constants extracted from the very fast OFDFT calculations, because such calculations are computationally challenging using KSDFT. This is especially the case for the $Mg_{23}Al_{30}$ compound, whose 3×3×3 supercell consists of 1431 atoms. We finally employ the quasi-harmonic approximation to investigate temperature-dependent thermodynamic properties, including formation energies, heat capacities, and thermal expansion of the four Mg-Al intermetallic compounds. The calculated heat capacity and thermal expansion of both Mg and Al agree well with experimental data. We additionally find that $Mg_{13}Al_{14}$ and $MgAl_2$ are both unstable, consistent with their absence from the equilibrium Mg-Al phase diagram. Our work demonstrates that OFDFT is an efficient and accurate quantum-mechanical computational tool for predicting elastic and thermodynamic properties of complicated Mg-Al alloys and also should applicable to many other engineering alloys.

Introduction

Magnesium (Mg) and aluminum (Al) are two of the most abundant metal elements on earth. Alloys based on these two elements exhibit a wealth of excellent properties such as low density and high strength-to-weight ratio, which lead to a variety of applications including lightweight automobile components and portable electronic devices [1]. An abundance of these elements combined with their potential to enhance energy-efficiency of vehicles via weight reduction encourages use of Mg-Al alloys far into the future.

Properties of Mg-Al alloys, particularly mechanical properties of primary engineering interest, strongly depend on diverse stoichiometric and nonstoichiometric intermetallic phases [2] that are commonly observed due to the chemically active nature of Mg. One representative example is that of the precipitated intermetallic compound $Mg_{17}Al_{12}$ that is responsible for creep deformation at high temperature, which subsequently deteriorates the performance of Mg-Al alloys [3]. Studies of Mg-Al intermetallics therefore are critical to improving Mg-Al alloy properties and ultimately widening the range of their applications.

Computational tools based on Kohn-Sham density functional theory (KSDFT) [4,5] play an important role in understanding Mg-Al intermetallic compounds. Numerous KSDFT calculations have characterized various properties of Mg-Al intermetallic compounds [6-9]. Elastic and thermodynamic properties are two of the most critical and of the greatest interest for engineering Mg-Al alloys. The former property indicates the stiffness of a material, while the latter property affects its phase stability at high temperatures. Both properties are measurable in experiment and computable in theory.

Methods based on atomic models to calculate elastic properties typically require a large number of energy calculations for an optimized cell that is subjected to different strain patterns. These calculations are time-consuming within KSDFT, especially for cells with low symmetries and consisting of many atoms. Similarly, phonon calculations usually involve supercells with a number of atomic displacements to determine thermodynamic properties [6]. Phonon calculations at the KSDFT level are limited to supercells with a small number of atoms because of the large number of operations needed that involve the KS orbitals at sufficiently sampled *k* points in reciprocal space. However, Mg-Al alloys contain complicated stoichiometric, *e.g.*, $Mg_{23}Al_{30}$ [10], and nonstoichiometric, *e.g.*, the Samson phase of Mg_2Al_3 [11], compounds with large unit cells that make KSDFT-derived phonon computations prohibitively expensive.

Orbital-free DFT (OFDFT), on the other hand, scales quasi-linearly with system size with a small prefactor and hence is significantly faster than the typical cubic scaling of KSDFT [12]. OFDFT and KSDFT methods differ in two fundamental respects. First, OFDFT describes the kinetic energy of electrons using a kinetic energy density functional (KEDF) [13], while KSDFT adopts KS orbitals to exactly evaluate the non-interacting electron kinetic energy. By eschewing orbitals, the electron density becomes the sole variable in OFDFT. This enormous simplification significantly increases the number of atoms that can be treated with DFT. Second, although non-local pseudopotentials (NLPSs) [14] are widely used in KSDFT to accurately describe electron-ion interactions, pure OFDFT utilizes local pseudopotentials (LPSs) because no orbitals are available to use with the orbital-based non-local projectors present in NLPSs. An LPS must be carefully constructed and tested. Here, we choose the bulk-derived LPSs (BLPSs) [15,16] for both Al and Mg [17].

OFDFT with suitable non-local KEDFs [18-24] and LPSs yields accurate properties of light metals and their compounds [25]. Examples include the motion of edge and screw dislocations in pure face-centered cubic (fcc) Al [26-28] and hexagonal-closest-packed (hcp) Mg [29,30], ductile crack propagation in fcc Al [31], diffusion of silicon along an edge dislocation of fcc Al [32], vacancy formation and aggregation in Al [33], melting behavior of sodium clusters [34], as well as plasticity properties of body-centered cubic Mg-Li alloys [35]. Bulk and vacancy formation energies of four Mg-Al intermetallic compounds, $Mg_{17}Al_{12}$, $Mg_{13}Al_{14}$, and $Mg_{23}Al_{30}$, and $MgAl_3$ [36], were recently studied with a real-space implementation of OFDFT [37].

In the present work, we focus on four stoichiometric compounds, *i.e.*, $Mg_{17}Al_{12}$, $Mg_{13}Al_{14}$, $Mg_{23}Al_{30}$, and $MgAl_2$, which have been experimentally observed and archived in the inorganic crystal structure database (ICSD) [38]. We first compare lattice constants calculated via OFDFT and KSDFT with those obtained from experiment. This comparison serves as a benchmark of the reliability of OFDFT and the chosen KEDF for simulating Mg-Al alloys. We next assess the stability of these four Mg-Al intermetallic structures by means of three common criteria: formation energies, elastic constants, and phonon dispersion. Our calculated elastic constants and Pugh's ratios suggest that $Mg_{23}Al_{30}$ and $MgAl_2$ should exhibit better ductility than $Mg_{17}Al_{12}$ and precipitates of the former could be used to improve the ductility of magnesium. We then use the phonon frequencies dispersed over the reciprocal lattice to obtain thermodynamic properties, including the temperature-dependent formation energy, constant-pressure heat capacity, and linear thermal expansion coefficients of the four intermetallic compounds. Our work offers the first predicted phonon spectra of $Mg_{23}Al_{30}$, $Mg_{13}Al_{14}$, and $MgAl_2$. It also provides another set of tests of the transferability of the Mg and Al BLPSs [16,17] and of the accuracy of the Wang-Teter (WT) KEDF [18] used in this study (*vide infra*). We demonstrate that OFDFT can be used as an independent (non-empirical) simulation tool for characterizing properties of and perhaps ultimately facilitating optimal design of Mg-Al alloys. In addition to light metal compounds with simple crystal structures [26-35], this simulation tool can be used to characterize the behavior of numerous other complicated alloys, for which experimental elastic and thermodynamic properties do not exist and for which theoretical data are too computationally expensive to obtain with, *e.g.*, KSDFT. Making these data available is critical for expediting development of new engineering alloys, *e.g.*, to pinpoint alloy compositions with desirable target properties. This objective is in line with the Materials Genome Initiative [39]. Tremendous effort has been expended collecting such large data sets of materials properties. For example, Asta and coworkers calculated the elastic properties of about 1200 inorganic compounds using KSDFT [40]. In this context, we will demonstrate that using our OFDFT method to compute elastic and thermodynamic properties is an extremely efficient technique to analyze, augment, and predict such properties, which will continue to expand currently available databases.

Methods

We used the Vienna *Ab Initio* Simulation Package (VASP) [41] to perform all KSDFT calculations. The projector augmented wave (PAW) method [42,43] was employed, with the standard PAW projectors for Mg and Al that respectively treat the outer two and three valence electrons self-consistently in the presence of all-electron frozen core atomic densities. We employed the Perdew-Burke-Ernzerhof (PBE) functional for electron exchange-correlation (XC) [44].

Figure 1 displays the crystal structures of $Mg_{17}Al_{12}$, $Mg_{13}Al_{14}$, $Mg_{23}Al_{30}$, and $MgAl_2$. The crystal structure data for these intermetallic phases with their respective identification (ID) numbers in the ICSD and space groups are listed in

Table 1 (*vide infra*). We used primitive cells for geometry relaxations and energy calculations of Mg, $Mg_{17}Al_{12}$, $Mg_{13}Al_{14}$, $Mg_{23}Al_{30}$, $MgAl_2$, and Al, consisting of 2, 29, 27, 53, 12, and 1 atoms, respectively. The Monkhorst-Pack *k*-point grids [45] used for these primitive cells were correspondingly 18 × 18 × 12, 8 × 8 × 8, 10 × 10 × 10, 8 × 8 × 8, 8 × 8 × 12, and 18 × 18 × 18. A 500 eV kinetic energy cutoff for the plane wave basis set was used. The selected planewave kinetic energy cutoff and *k*-point meshes ensured that the accuracy of the total energy is converged to within 1.0 meV/atom. Integration over the Brillouin zone was performed using the Methfessel-Paxton [46] method with a smearing width of 0.2 eV. All lattice parameters and atomic coordinates were fully relaxed until a force tolerance of 0.01eV/Å was reached.

All OFDFT calculations were performed using the PROFESS 3.0 package [47]. The total energy functional within the OFDFT scheme is an electron-density-only functional and thus no explicit orbitals are needed:

$$E_{tot}\left[\rho(r)\right]=T_s\left[\rho(r)\right]+\frac{1}{2}\int\int\frac{\rho(r)\rho(r')}{|r-r'|}drdr'+\int\varphi_{IE}(r)\rho(r)dr+E_{xc}\left[\rho(r)\right]+E_{II} \tag{1}$$

where the first term is the KEDF of a real-space electron density $\rho(r)$. We adopted the WT KEDF [18], which is based on the Lindhard response function for the perturbed uniform electron gas, as this response function contains the physics appropriate for studying nearly-free-electron-like metals such as Mg and Al and their alloys. Our group has previously shown that the WT KEDF and the more recent Wang-Govind-Carter (WGC) [22,24] KEDF yield nearly the same lattice constants, elastic moduli and total energies for hcp Mg and fcc Al [36]. In Ref. [48], we further compare the phonon spectra calculated with these two nonlocal KEDFs. The two phonon spectra are reasonably independent of the choice of KEDF. However, when applied to the Mg-Al alloys, the WGC KEDF suffers from a numerical instability problem originating from the second order Taylor expansion used in the WGC expression [49]. We therefore use the WT KEDF throughout this work. The second and third terms in Eq. (1) represent the electron-electron Coulomb repulsion and ion-electron interactions, respectively. The latter is evaluated using the BLPSs mentioned earlier [17]. The final two terms in Eq. (1) respectively denote the XC and ion-ion interactions, with the PBE functional used for the XC term. We used a plane wave basis kinetic energy cutoff of 1200 eV here in OFDFT in order to reach the same convergence as for the PAW potentials employed in KSDFT. The

PAW potentials utilize a smooth electron density on a uniform grid which then permits a lower kinetic energy cutoff, while the BLPSs are somewhat sharper functions, requiring a higher cutoff to achieve the same accuracy. We used the truncated Newton method [50,51] for optimizing the electron density, with the initial guess density being that of a uniform electron gas. All geometries are fully relaxed with the conjugate gradient method until the forces reach the tolerance of 5×10^{-5} hartree-bohr^{-1}, *i.e.*, 2.6 meV/Å.

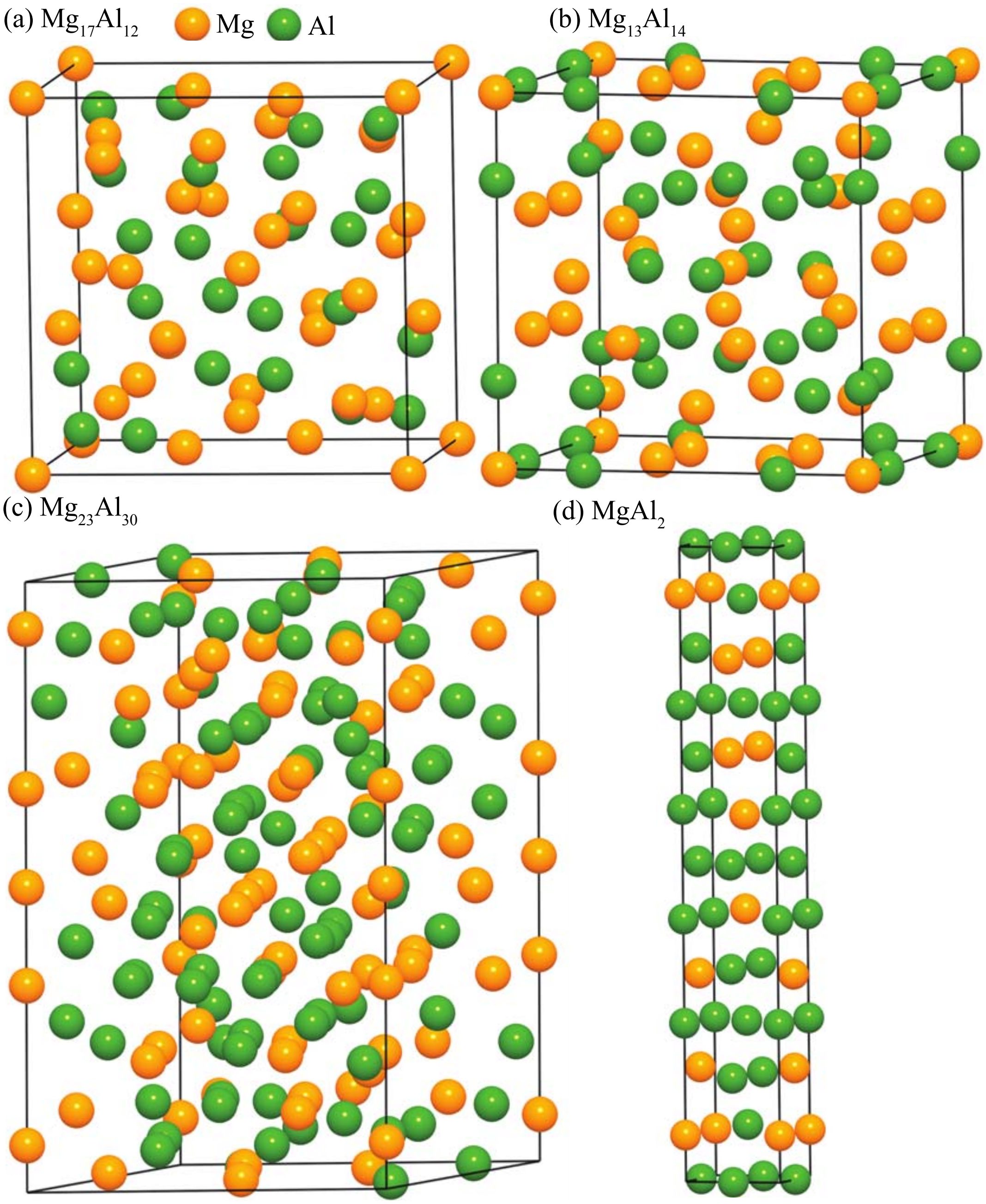

Figure 1. Schematic representation of (a) $Mg_{17}Al_{12}$, (b) $Mg_{13}Al_{14}$, (c) $Mg_{23}Al_{30}$, and (d) $MgAl_2$ crystal structures.

We used the strain-energy method to obtain the independent elastic constants of hcp Mg, fcc Al, and the four Mg-Al intermetallic compounds [52,53]. We apply a series of strains to an optimized unit cell, and the atomic positions are fully relaxed until the force tolerance is reached. A general applied strain □ is written as

$$\varepsilon = \left(\varepsilon_{11}, \varepsilon_{22}, \varepsilon_{33}, 2\varepsilon_{23}, 2\varepsilon_{31}, 2\varepsilon_{12}\right) \tag{2}$$

with the elements □$_{ij}$ (i, j = 1, 2, 3) defined as

$$\varepsilon_{ij} = \frac{1}{2}\left(\frac{\partial u_i}{\partial x_j} + \frac{\partial u_j}{\partial x_i}\right) \tag{3}$$

where u is the displacement at point x.

Under this strain, the resulting strain energy is

$$\Delta E = E - E_0 = U \cdot V \tag{4}$$

where E and E_0 are the energies of the deformed and strain-free cells, respectively, and V is the volume of the deformed cell. U is the strain energy density under each strain:

$$U = \frac{1}{2}\varepsilon \cdot C \cdot \varepsilon \tag{5}$$

where C is the stiffness tensor in the Voigt notation [54]. The calculated strain energy density as a function of the applied strain is quadratically fitted to obtain the above individual elastic constants. We used energy data corresponding to 20 strains δ ranging from -1.0% to 1.0% with an increment of 0.1% in the present work. The number of independent elastic constants in the stiffness tensor for hexagonal, cubic, trigonal, and tetragonal crystal systems is different depending on the crystal symmetry. We provide the details of strain patterns applied to each crystal system in Ref. [48].

We implemented a Python-based interface to calculate the phonon spectra by coupling PROFESS 3.0 with PHONOPY [55,56]. We first used this interface to generate supercells of various Mg-Al alloys based on their symmetries. We utilized 6 × 6 × 6 supercells for hcp Mg and fcc Al, where the numbers multiply the primitive unit cells discussed earlier to create the supercell. We built 3 × 3 × 3 supercells for $Mg_{17}Al_{12}$, $Mg_{13}Al_{14}$, $Mg_{23}Al_{30}$, and $MgAl_2$. This notably results in 53 $Mg_{23}Al_{30}$ supercells, each of which corresponds to an inequivalent pattern of atomic displacement (determined by the symmetry of $Mg_{23}Al_{30}$) and consists of 1431 atoms. We employed PROFESS 3.0 to perform static energy calculations for each supercell that yields atomic forces that are collected by the PROFESS 3.0-PHONOPY interface. The interface post-processes the atomic forces and transforms them to force constants using the PHONOPY package [55,56] with 53 inequivalent displacements. The large number of phonon bands obscures observation, so we also calculated the corresponding phonon densities of states with the same *k*-point density as used in the KSDFT calculations and with a broadening parameter of 2 cm^{-1}.

We adopted the quasi-harmonic approximation (QHA) [57] for the thermodynamic properties calculations, including temperature (T) - dependent formation energies $E_\mathrm{f}(T)$, heat capacities at constant pressure $C_P(T)$, and linear thermal expansion coefficients $\alpha_L(T)$, where quasi-harmonic effects are taken into account by computing volume (V) -dependent phonon frequencies $\omega(\vec{q},V)$ with $\vec{q}$ being the phonon wave vector. The contributions of lattice vibrations $A(V,T)$ to the Helmholtz free energy $F(V,T)$ within the QHA, are given by [57]

$$A(V,T)=\frac{1}{2}\sum_{\vec{q}}\hbar\omega(\vec{q},V)+k_\mathrm{B}T\sum_{\vec{q}}\ln\left[1-\exp\left\{-\frac{\hbar\omega(\vec{q},V)}{k_\mathrm{B}T}\right\}\right] \tag{6}$$

Therefore,

$$F(V,T)=E_0(V)+A(V,T) \tag{7}$$

where E_0 (V) is the quantum mechanical total energy of a system with volume V. Minimizing $F(V, T)$ with respect to V at a specified T gives the Helmholtz free energy at that temperature. Then,

$$E_{\mathrm{f}}(T) = \Delta F(V,T) = \left\{ F_{\mathrm{Mg_xAl_y}}(T) - xF_{\mathrm{Mg}}(T) - yF_{\mathrm{Al}}(T) \right\} / (x+y) \tag{8}$$

where $F_{\mathrm{MgxAly}}(T)$, $F_{\mathrm{Mg}}(T)$, and $F_{\mathrm{Al}}(T)$ refer to the Helmholtz free energies of an $\mathrm{Mg}_x\mathrm{Al}_y$ intermetallic compound, hcp Mg, and fcc Al, respectively. x and y respectively denote the number of Mg and Al atoms in $\mathrm{Mg}_x\mathrm{Al}_y$.

To calculate $C_P(T)$ and $\alpha_L(T)$ at zero pressure ($P = 0$), we employed the relation [57,58]

$$C_P(T) = C_V(T) + \alpha_V^2(T)B(T)VT \tag{9}$$

where C_V(T) is the constant volume heat capacity

$$C_V(T) = -T\left(\frac{\partial^2 F(V,T)}{\partial T^2}\right)_V \quad , \tag{10}$$

$B(V, T)$ is the bulk modulus

$$B(V,T) = V\left(\frac{\partial^2 F(V,T)}{\partial V^2}\right)_T \quad , \tag{11}$$

and $\alpha_V(T)$ is the volume thermal expansion coefficient

$$\alpha_V(T) = \frac{1}{V}\left(\frac{\partial V}{\partial T}\right)_P \quad . \tag{12}$$

The linear thermal expansion coefficient $\alpha_L(T)$ depends on $\alpha_V(T)$ as

$$\alpha_L(T) = \frac{1}{3}\alpha_V(T) \ . \tag{13}$$

To obtain $\omega(\vec{q},V)$, we calculate the phonon frequencies for each intermetallic compound at 17 different volumes ranging from 0.94 to 1.06V_0, where V_0 is the equilibrium volume of a ground-state structure. This requires, *e.g.*, 901 static energy calculations for the 1431-atom $Mg_{23}Al_{30}$ supercell, not feasible for KSDFT but easily done within OFDFT. A grid of 24 × 24 × 24 q points on the reciprocal lattice was utilized for the summation in Eq. (6).

Results and discussion

Table 1 lists the predicted equilibrium lattice constants of hcp Mg, $Mg_{17}Al_{12}$, $Mg_{13}Al_{14}$, $Mg_{23}Al_{30}$, $MgAl_2$, and fcc Al using both OFDFT and KSDFT. Experimental and theoretical data from the literature are also given for comparison. We observe satisfactory agreement between our simulation results and those from the literature. Our OFDFT and KSDFT lattice constants compare well; in some cases the results from OFDFT are fortuitously slightly closer to experimental values, *e.g.*, the lattice constant of $Mg_{13}Al_{14}$ (10.314 Å) obtained from OFDFT is closer to the experimental value (10.437 Å) than the KSDFT result (10.183 Å).

We next consider the formation energy E_f of an Mg_xAl_y compound at zero Kelvin according to

$$E_{\mathrm{f}} = \left(E_{\mathrm{Mg}_x\mathrm{Al}_y} - xE_{\mathrm{Mg}} - yE_{\mathrm{Al}} \right) / (x+y) \quad \textbf{(14)}$$

where $E_{\mathrm{Mg}_x\mathrm{Al}_y}$, E_{Mg}, and E_{Al} refer to the ground-state total energies per formula unit of $\mathrm{Mg}_x\mathrm{Al}_y$, hcp Mg, and fcc Al cells, respectively. This definition is analogous to that of the temperature-dependent formation energy given in the previous section (Eq. (8)). Negative E_{f}s correspond to stable Mg-Al intermetallic compounds, and vice versa for positive E_{f}s. Table 1 lists the E_{f}s derived from OFDFT and KSDFT, along with previous theoretical and experimental data for comparison. Our OFDFT and KSDFT formation energies once again agree reasonably well with each other, to within 20 meV/atom. These energies are also consistent with other theoretical reference values, *e.g.*, the E_{f} of $\mathrm{Mg}_{17}\mathrm{Al}_{12}$ calculated with both OFDFT and KSDFT lie within a wide span of literature results ranging from -48 to -11 meV/atom.

Among the four Mg-Al intermetallic compounds, $\mathrm{Mg}_{17}\mathrm{Al}_{12}$ and $\mathrm{Mg}_{23}\mathrm{Al}_{30}$ are the only ones that exhibit negative E_{f}s, which shows that these two structures are stable at zero Kelvin. The magnitudes of E_{f} for these two compounds are also close. In contrast, the predicted E_{f}s of $\mathrm{Mg}_{13}\mathrm{Al}_{14}$ and MgAl_2 are positive, suggesting that they are unstable at zero Kelvin, *i.e.*, the decomposition of these two compounds to hcp Mg and fcc Al is exothermic. We also observe that the E_{f} of $\mathrm{Mg}_{13}\mathrm{Al}_{14}$ is much larger than that of MgAl_2, indicating $\mathrm{Mg}_{13}\mathrm{Al}_{14}$ is much less stable than MgAl_2 at zero Kelvin. As we will see later, the contrasting E_{f}s of $\mathrm{Mg}_{13}\mathrm{Al}_{14}$ and MgAl_2 are consistent with their phonon spectra: $\mathrm{Mg}_{13}\mathrm{Al}_{14}$ has imaginary frequencies while MgAl_2 has only real ones.

Table 1. Crystal structure information including ICSD ID, structure, space group, and lattice constants *a* and *c*/*a* of hcp Mg, $Mg_{17}Al_{12}$, $Mg_{13}Al_{14}$, $Mg_{23}Al_{30}$, $MgAl_2$, and fcc Al. Zero-Kelvin formation energies E_f of $Mg_{17}Al_{12}$, $Mg_{13}Al_{14}$, $Mg_{23}Al_{30}$, and $MgAl_2$. Experimental and theoretical data from the literature are also shown for comparison. Results calculated in this work are shown in bold, while experimental data are italicized. Literature KSDFT data are shown in regular font.

	ICSD ID	Structure	Space group	*a* (Å)	*c*/*a*	E_f (meV/atom)
hcp Mg	76748	Hexagonal	No. 194, $P6_3/mmc$	**3.195**[a] **3.192**[b] *3.209*[c]	**1.632**[a] **1.623**[b] *1.624*[c]	
$Mg_{17}Al_{12}$	158247	Cubic	No. 217, $I\bar{4}3m$	**10.649**[a] **10.523**[b] *10.549*[d] 10.55[f] 10.53[g] 10.571[h]		**-35.5**[a] **-24.3**[b] -11.0[e] -48[f] -27[g] -21[h]
$Mg_{13}Al_{14}$	150647	Cubic	No. 229, $Im\bar{3}m$	**10.314**[a] **10.183**[b] *10.437*[i]		**42.7**[a] **61.6**[b] 52[e]
$Mg_{23}Al_{30}$	57965	Trigonal	No. 148, $R\bar{3}$	**12.966**[a] **12.790**[b] *12.825*[j]	**1.670**[a] **1.692**[b] *1.696*[j]	**-34.6**[a] **-18.7**[b] -34[e]
$MgAl_2$	608412	Tetragonal	No. 141, $I4_1/amd$	**4.236**[a] **4.195**[b] *4.132*[k]	**5.979**[a] **5.955**[b] *6.438*[k]	**18.7**[a] **11.9**[b]
fcc Al	43423	Cubic	No. 225, $Fm\bar{3}m$	**4.063**[a] **4.039**[b] *4.050*[l]		

[a] OFDFT; this work.
[b] KSDFT; this work.
[c] Experiment; reference [59].
[d] Experiment; reference [60].
[e] OFDFT; reference [37].
[f] KSDFT; reference [61].

[g] KSDFT; reference [6].
[h] KSDFT; reference [9].
[i] Experiment; reference [62].
[j] Experiment; reference [10].
[k] Experiment; reference [63].
[l] Experiment; reference [64].

The formation energy is only the first basic criterion of structural stability. We proceed to evaluate another important criterion, the mechanical stability [65], that can be directly determined from the calculated elastic constants (Table 2). As shown in the table, our calculated elastic constants of hcp Mg and fcc Al are in fair agreement with available experimental data. Additionally, the OFDFT elastic constants of Mg, $Mg_{17}Al_{12}$, and Al generally are very close to KSDFT results from the current and previous work, with the lone exception being C_{12} of $Mg_{17}Al_{12}$, which has a larger discrepancy.

Table 2. Elastic constants (in GPa) and Pugh's ratio B/G of hcp Mg, $Mg_{17}Al_{12}$, $Mg_{13}Al_{14}$, $Mg_{23}Al_{30}$, $MgAl_2$, and fcc Al. Experimental and theoretical data from the literature are also shown for comparison. Results calculated in this work are shown in bold, while experimental data are italicized. Literature KSDFT data are shown in regular font. The B/G of $Mg_{13}Al_{14}$ is not shown because $Mg_{13}Al_{14}$ is mechanically unstable.

	C_{11}	C_{12}	C_{13}	C_{14}	C_{15}	C_{33}	C_{44}	C_{66}	B/G
hcp Mg	**63**[a] **66**[b] *64*[c]	**28**[a] **25**[b] *26*[c]	**21**[a] **19**[b] *22*[c]			**67**[a] **70**[b] *66*[c]	**15**[a] **20**[b] *18*[c]		**2.118**[a] **1.714**[b] *1.932*[c]
$Mg_{17}Al_{12}$	**94**[a] **96**[b] 87[d] 98[e] 88[f] 91[g]	**18**[a] **27**[b] 29[d] 28[e] 24[f] 27[g]					**20**[a] **22**[b] 20[d] 31[e] 27[f] 30[g]		**1.671**[a] **1.897**[b] 2.081[d] 1.577[e] 1.569[f] 1.570[g]
$Mg_{13}Al_{14}$	**37**[a] **45**[b]	**46**[a] **51**[b]					**24**[a] **38**[b]		
$Mg_{23}Al_{30}$	**79**[a] **78**[b]	**38**[a] **46**[b]	**38**[a] **45**[b]	**2**[a] **3**[b]	**0**[a] **2**[b]	**78**[a] **79**[b]	**26**[a] **18**[b]		**2.300**[a] **3.380**[b]
$MgAl_2$	**73**[a] **82**[b]	**45**[a] **50**[b]	**44**[a] **48**[b]			71[a] **84**[b]	**23**[a] **19**[b]	**25**[a] **27**[b]	**2.800**[a] **3.077**[b]
fcc Al	**100**[a] **103**[b] 106[h] *107*[i]	**69**[a] **66**[b] 57[h] *61*[i]					**30**[a] **33**[b] 28[h] *28*[i]		**3.447**[a] **2.994**[b] 2.763[h] *2.950*[i]

[a] OFDFT; this work.
[b] KSDFT; this work.
[c] Experiment; reference [66].
[d] KSDFT; reference [61].
[e] KSDFT; reference [6].
[f] KSDFT; reference [7].
[g] KSDFT; reference [9].
[h] KSDFT; reference [67].
[i] Experiment; reference [68].

Notably, we find that C_{14} and C_{15} of $Mg_{23}Al_{30}$ are significantly smaller than the other components of the stiffness tensor. In the four-index notation, these two elastic constants can be written as

$$C_{14} = C_{1123} = \frac{\sigma_{11}}{\varepsilon_{23}} \tag{15}$$

and

$$C_{15} = C_{1131} = \frac{\sigma_{11}}{\varepsilon_{31}} \tag{16}$$

We conclude that a small stress σ_{11} along the *x* direction for $Mg_{23}Al_{30}$ will cause significant shear strains $\square_{23}$ and $\square_{31}$ on the *yz* and *zx* planes, respectively.

We employ Born's stability criteria [69] to examine the mechanical stability of these materials, which exploits the idea that any applied strain should increase the energy of a stable, ground-state solid. Numerically, the stiffness tensor must be positive definite [70]; namely, the eigenvalues of this matrix are all positive. The elastic constants of crystals should fulfill certain conditions based on their different symmetries as a result [71]. More precisely, the following four criteria have to be satisfied for hcp Mg and tetragonal $MgAl_2$ [71]:

$$C_{11} > \left|C_{12}\right| \tag{17}$$

$$2C_{13}^2 < C_{33}\left(C_{11} + C_{12}\right) \tag{18}$$

$$C_{44} > 0 \tag{19}$$

and

$$C_{66} > 0 \tag{20}$$

Substitution of OFDFT and KSDFT elastic constants into the above relations confirms that hcp Mg and $MgAl_2$ are mechanically stable. For cubic $Mg_{17}Al_{12}$, $Mg_{13}Al_{14}$, and fcc Al, three criteria need to be met:

$$C_{11} - C_{12} > 0 \tag{21}$$

$$C_{11} + 2C_{12} > 0 \tag{22}$$

and

$$C_{44} > 0 \tag{23}$$

We find that C_{11} and C_{12} of $Mg_{13}Al_{14}$ calculated from both KSDFT and OFDFT do not satisfy the above criteria whereas those of $Mg_{17}Al_{12}$ and fcc Al do. This finding is consistent with the large positive formation energy of $Mg_{13}Al_{14}$. Finally, the elastic constants should be commensurate with the following conditions for trigonal $Mg_{23}Al_{30}$ [71]:

$$C_{11} > \left|C_{12}\right| \tag{24}$$

$$C_{44} > 0 \tag{25}$$

$$2C_{13}^2 < C_{33}\left(C_{11} + C_{12}\right) \tag{26}$$

and

$$2C_{14}^2 < C_{44}\left(C_{11} - C_{12}\right) \tag{27}$$

It is straightforward to verify that all OFDFT and KFDFT elastic constants of $Mg_{23}Al_{30}$ comply with the above four conditions, confirming that $Mg_{23}Al_{30}$ is mechanically stable, although it may easily deform via shear, as mentioned earlier.

The elastic constants calculated above are useful not only for assessing the fundamental stability of the Mg-Al intermetallic compounds but also for evaluating mechanical properties of key interest for engineering applications. For instance, the elastic constants can be transformed to bulk moduli *B* and shear moduli *G* according to the Voigt-Reuss-Hill approximation (see Refs. [48,68]). Pugh found that the ratio *B*/*G* is strongly correlated to the ductility of a material, *i.e.*, a larger *B*/*G* indicates a better ductility [72]. The OFDFT *B*/*G* values for hcp Mg and fcc Al are in good agreement with available experimental values (Table 2). Furthermore, the OFDFT Pugh's ratios in Table

2 suggest that both $Mg_{23}Al_{30}$ and $MgAl_2$ should be more ductile than $Mg_{17}Al_{12}$, consistent with the brittle nature of the latter [73], and that precipitates of $Mg_{23}Al_{30}$ or $MgAl_2$ in Mg could improve its ductility. Thus, efficient screening of simple mechanical properties of complex Mg-Al intermetallic compounds is possible with OFDFT.

In addition to mechanical stability, we further assess another crucial criterion of stability, namely, phonon or dynamical stability [74]. The absence of imaginary phonon modes implies that a system is dynamically stable. We first benchmark our computed phonon spectra of hcp Mg and fcc Al obtained from OFDFT with those from KSDFT and measurements. Figure 2 displays the phonon spectra of hcp Mg and fcc Al from all three methods. We observe good agreement at most q points in the first Brillouin zone, when comparing phonon spectra from OFDFT with the ones from KSDFT and with experiment. However, we also observe that at other q points, *e.g.*, the X point for fcc Al, the OFDFT optical phonon frequency is around 30 cm^{-1} lower than the KSDFT one and the experimental data. This deviation shows the accuracy limits of the WT KEDF and/or the BLPSs used in OFDFT.

Phonon spectra for the four Mg-Al compounds considered here have not yet been measured. Figure 3 provides predicted phonon spectra of $Mg_{17}Al_{12}$, $Mg_{13}Al_{14}$, $Mg_{23}Al_{30}$, and $MgAl_2$. We emphasize that our calculated phonon spectra of $Mg_{13}Al_{14}$, $Mg_{23}Al_{30}$, and $MgAl_2$ are the first to ever be calculated at the DFT level. These calculations are only possible because of the speed and accuracy of OFDFT. Figure 3 also displays the corresponding phonon density of states (PDOS) in order to better visualize the distribution of phonon modes. We observe many flat phonon bands, which give rise to sharp peaks in the PDOS plots. The phonon modes for $Mg_{17}Al_{12}$ and $Mg_{23}Al_{30}$ in the first

Brillouin zone are all real, consistent with their negative formation energies and their elastic constants that satisfy Born's criteria. In contrast, $Mg_{13}Al_{14}$ exhibits imaginary phonon modes, suggesting that it is dynamically unstable, consistent with its positive formation energy and elastic constants failing to obey Born's criteria. Interestingly, although the zero-Kelvin formation energy of $MgAl_2$ is positive, the calculated phonon spectrum suggests that $MgAl_2$ is dynamically stable. The latter finding is also consistent with the elastic constants that we showed satisfy the Born criteria.

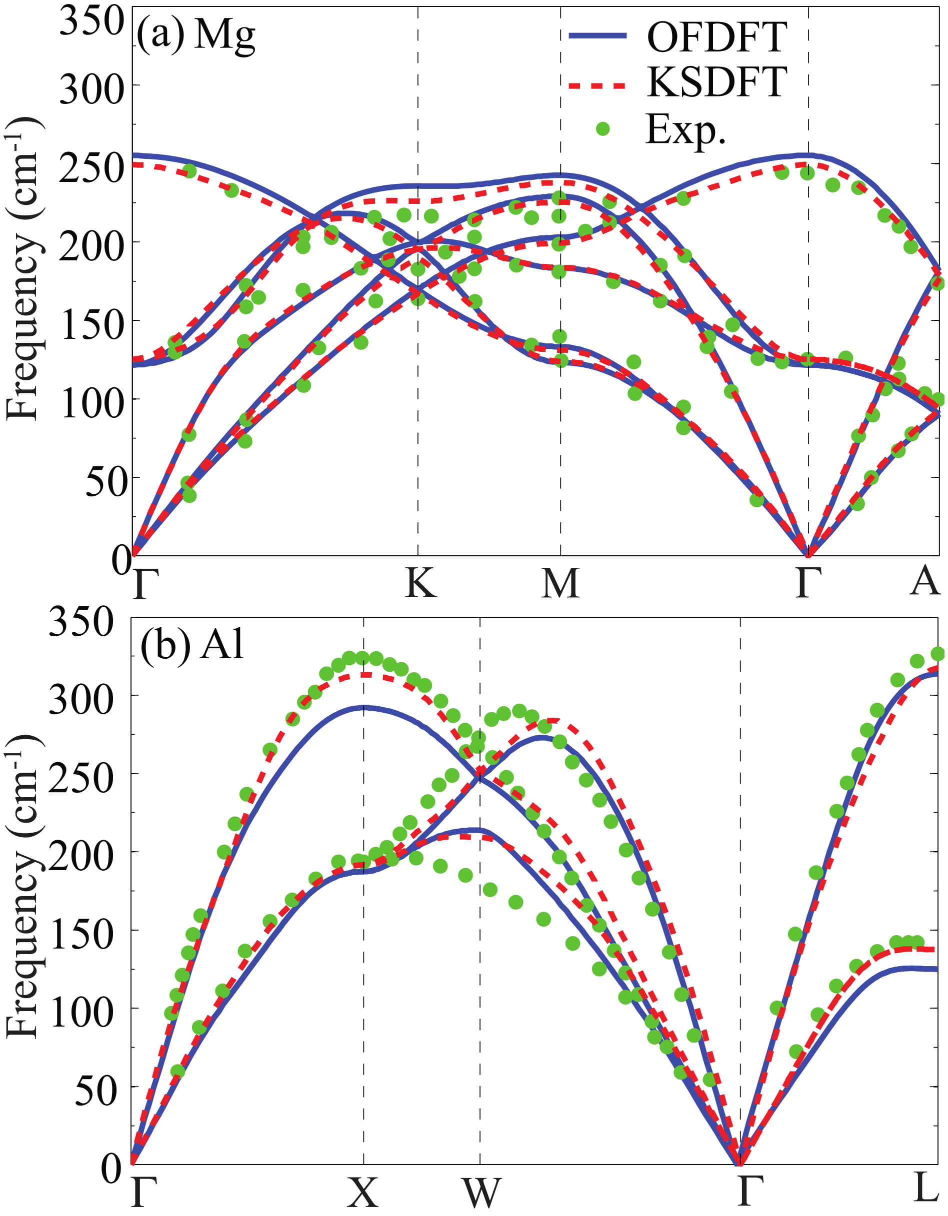

Figure 2. Phonon spectra of (a) hcp Mg and (b) fcc Al derived from OFDFT and KSDFT. Experimental data from Refs. [75] and [76] are also shown for comparison. The coordinates of the high-symmetry *q* points are Γ(0,0,0), K(1/3,1/3,0), M(0,1/2,0), A(0,0,1/2), X(0,1/2,1/2), W(1/4,3/4,1/2), and L(1/2,1/2,1/2), respectively.

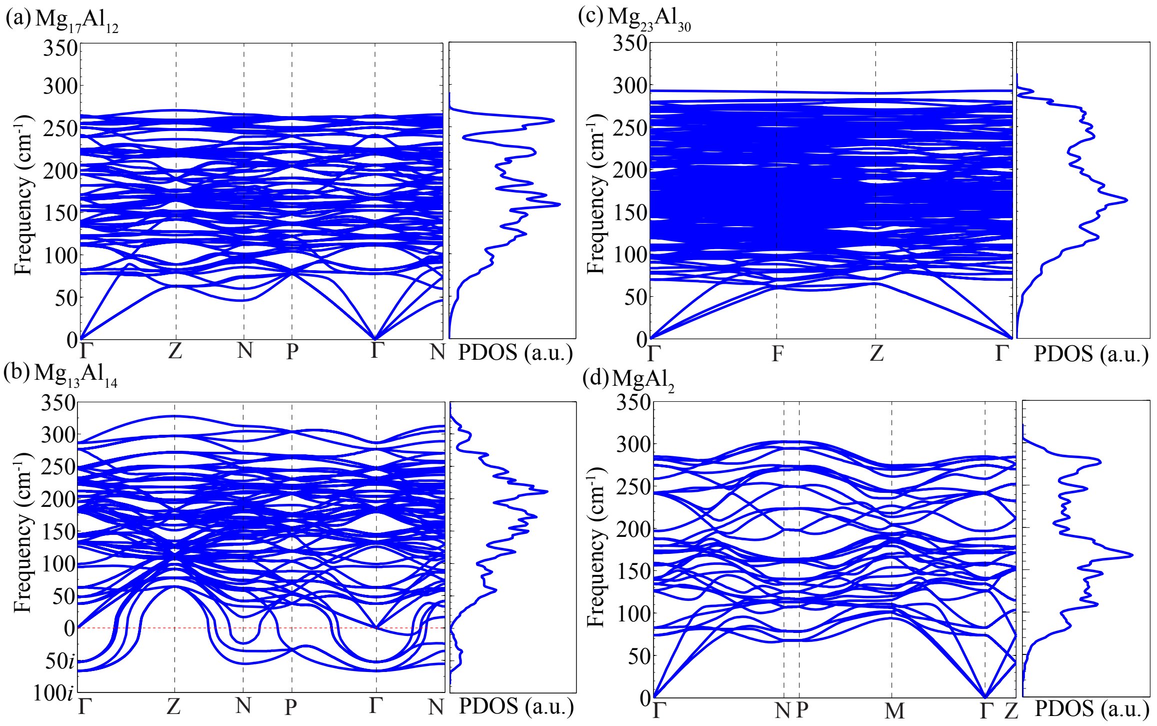

Figure 3. Phonon spectra and phonon density of states (PDOS) of (a) $Mg_{17}Al_{12}$, (b) $Mg_{13}Al_{14}$, (c) $Mg_{23}Al_{30}$, and (d) $MgAl_2$ calculated with OFDFT. The coordinates of the high-symmetry *q* points are Γ(0,0,0), Z(1/2,1/2,1/2), N(0,0,1/2), P(1/4,1/4,1/4), F(1/2,1/2,0), and M(0,1/2,0), respectively.

With the phonon dispersion relations now determined, we are able to explore how temperature affects the formation energy and other thermodynamic properties of the four Mg-Al intermetallic compounds. Figure 4(a) displays the formation energies of $Mg_{17}Al_{12}$, $Mg_{13}Al_{14}$, $Mg_{23}Al_{30}$, and $MgAl_2$ as a function of temperature. The formation energies decrease as temperature increases because of increasing phonon entropy as temperature rises. The formation energies of $Mg_{17}Al_{12}$ and $Mg_{23}Al_{30}$ are negative over the entire temperature range considered (0 K < T < 700 K, with the latter close to the melting temperature of $Mg_{17}Al_{12}$) [2], showing that they are thermally stable. This stability explains why both phases appear in the Mg-Al phase diagram [77]. In contrast, the formation energies of $Mg_{13}Al_{14}$ and $MgAl_2$ are much higher. The formation energy of $Mg_{13}Al_{14}$ remains completely positive (and dynamically unstable) at high temperatures while $MgAl_2$ is also unstable up to nearly 700 K. This instability correlates with the fact that both $MgAl_2$ and $Mg_{13}Al_{14}$ are absent from the equilibrium phase diagram. Indeed, the $MgAl_2$ phase has only been prepared by the liquisol quenching method [63], a common technique for obtaining non-equilibrium phases through rapid quenching of an alloy from the liquid to the solid state [78].

Finally, we use OFDFT to calculate thermodynamic properties of hcp Mg, $Mg_{17}Al_{12}$, $Mg_{13}Al_{14}$, $Mg_{23}Al_{30}$, $MgAl_2$, and fcc Al. In particular, we evaluate the constant pressure heat capacity C_P and the linear thermal expansion coefficient α_L, both of which are measureable quantities that can be directly compared to our predictions. OFDFT-derived C_P curves (Figure 4(b)) capture the typical variation of C_P with temperature, *i.e.*, strong and weak temperature dependence at low and high temperatures, respectively, resembling the Debye model [79]. The C_Ps of the six materials are predicted to have very similar values over a wide temperature range, reflecting the insensitivity of C_P in Mg, Al, and their respective alloys. Figure 4(c) displays the OFDFT-derived α_L values of the six materials. The calculated α_Ls of Mg and Al are nearly identical and in good agreement with experimental values. For example, at room temperature ($T = 298$ K), the calculated α_Ls of Mg and Al are 22.8 and 22.6×10^{-6}/K, respectively, quite close to the corresponding experimental values of 24.8 and 23.1×10^{-6}/K [80]. The four Mg-Al intermetallic compounds are predicted to exhibit larger α_Ls, especially at high temperatures. These differences potentially may affect interface properties, *e.g.*, misfit strain, when such an Mg-Al intermetallic phase precipitates from Mg at high temperatures.

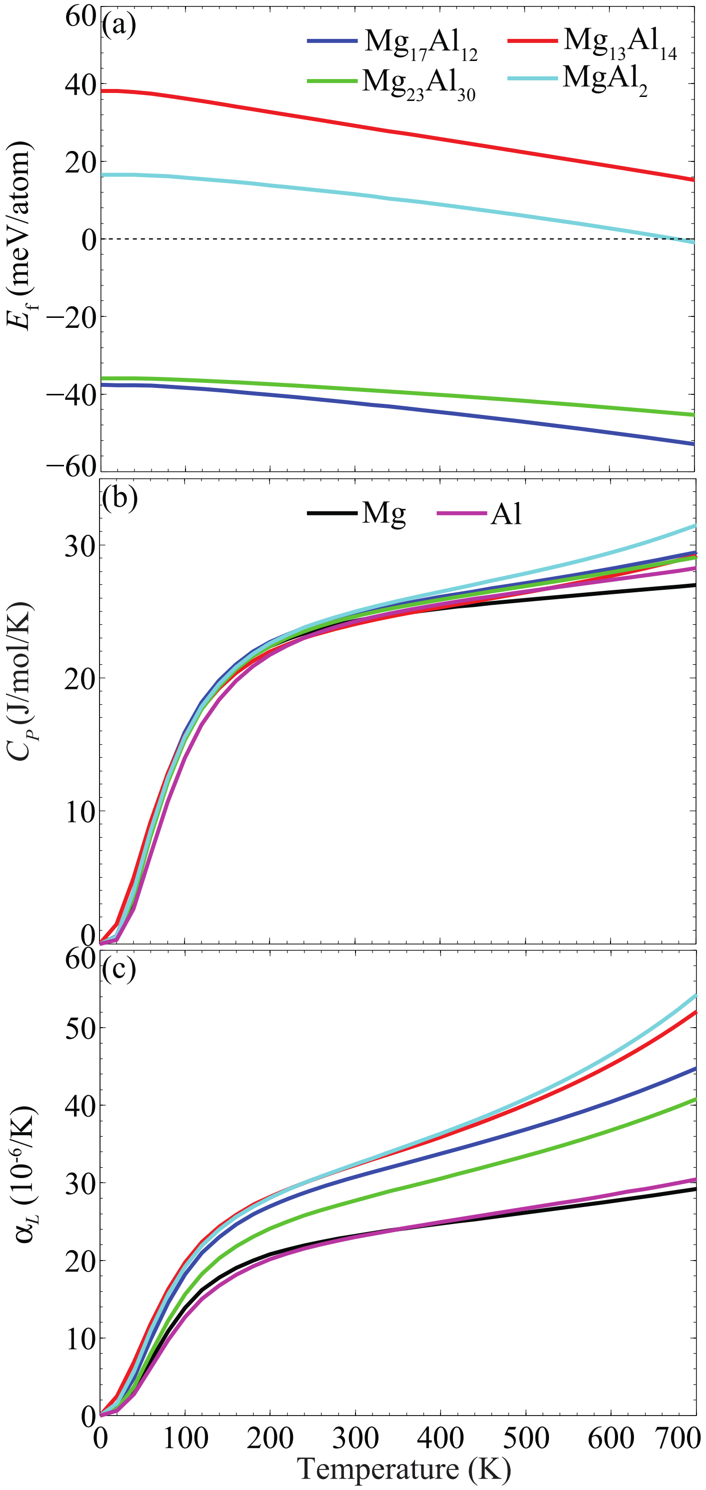

Figure 4. OFDFT-derived temperature-dependent (a) formation energies E_f, (b) heat capacities C_P, and (c) linear expansion coefficients α_L of four Mg-Al alloys. Temperature-dependent heat capacities and linear expansion coefficients for hcp Mg and fcc Al are also shown.

Conclusions

We computationally characterized various properties of four complex Mg-Al intermetallic compounds, including lattice constants, formation energies, and elastic constants. Benchmark computations performed on hcp Mg and fcc Al demonstrated that OFDFT with the nonlocal WT KEDF is as accurate as KSDFT for Mg-Al intermetallics. The extraordinary computational efficiency of OFDFT permitted phonon spectra and thermodynamic properties of the four Mg-Al intermetallic compounds to be obtained. In particular, the phonon spectra and thermodynamic properties of $Mg_{23}Al_{30}$, $Mg_{13}Al_{14}$, and $MgAl_2$ were predicted for the first time, offering explanations of prior and guidance to future experiments. For example, $Mg_{13}Al_{14}$ and $MgAl_2$ were predicted to have positive formation energies, consistent with their absence from the experimental phase diagram of Mg-Al alloys. Secondly, the predicted differences in thermal expansion coefficients of the intermetallic compounds suggest that possible interfacial strains may emerge during high temperature metallurgical processing of Mg-Al alloys. From the theoretical perspective, our work shows that the WT KEDF combined with the BLPS within the OFDFT framework is quantitatively reliable and very efficient for computing different properties of Mg-Al intermetallic compounds.

From a broader perspective, our procedure for characterizing the elastic and thermodynamic properties of Mg-Al intermetallic compounds via OFDFT can be straightforwardly generalized to study the properties and behavior of other complicated Mg-Al intermetallic compounds and many other lightweight alloys. We plan to link our method to the ICSD so that complex intermetallic structures documented in the database can be used as starting points for automatic OFDFT calculations. This high-throughput strategy will establish a database of elastic constants and thermodynamic properties of complicated intermetallic compounds. Such an OFDFT-based database will extend existing ones such as the KSDFT-based Materials Project [81]. The resulting database will serve as a map of alloy selection and ultimately to accelerate discovery of new lightweight alloys for applications in the automotive and portable electronic device industries.

Acknowledgements

We are grateful to the Office of Naval Research for funding (Grant No. N00014-15-1-2218). We acknowledge use of the TIGRESS high performance computer center at Princeton University. We thank Ms. Nari Baughman and Dr. Johannes M. Dieterich for critical reading of this manuscript.

References

[1] I. Polmear and D. S. John, *Light Alloys : From Traditional Alloys to Nanocrystals* (Butterworth-Heinemann, 2005), 4 edn.
[2] N. Hort, Y. Huang, and K. U. Kainer, Intermetallics in magnesium alloys, Adv. Eng. Mater. **8**, 235 (2006).
[3] A. I. Taub and A. A. Luo, Advanced lightweight materials and manufacturing processes for automotive applications, MRS Bull. **40**, 1045 (2015).
[4] P. Hohenberg and W. Kohn, Inhomogeneous electron gas, Phys. Rev. **136**, B864 (1964).
[5] W. Kohn and L. J. Sham, Self-consistent equations including exchange and correlation effects, Phys. Rev. **140**, A1133 (1965).
[6] H. Zhang, S. L. Shang, Y. Wang, A. Saengdeejing, L. Q. Chen, and Z. K. Liu, First-principles calculations of the elastic, phonon and thermodynamic properties of $Al_{12}Mg_{17}$, Acta Mater. **58**, 4012 (2010).
[7] Z. W. Huang, Y. H. Zhao, H. Hou, and P. D. Han, Electronic structural, elastic properties and thermodynamics of $Mg_{17}Al1_2$, Mg_2Si and Al_2Y phases from first-principles calculations, Physica B **407**, 1075 (2012).
[8] H. L. Chen, L. Lin, P. L. Mao, and Z. Liu, Phase stability, electronic, elastic and thermodynamic properties of Al-RE intermetallics in Mg-Al-RE alloy: A first principles study, J. Magnesium Alloys **3**, 197 (2015).
[9] W.-C. Hu *et al.*, Predictions of mechanical and thermodynamic properties of $Mg_{17}Al_{12}$ and Mg_2Sn from first-principles calculations, Philos. Mag. **95**, 1626 (2015).

[10] S. Samson and E. K. Gordon, The crystal structure of epsilon-$Mg_{23}Al_{30}$, Acta Crystallogr., Sect. B **24**, 1004 (1968).
[11] S. Samson, The crsytal structure of the phase beta Mg_2Al_3, Acta Crystallogr. **19**, 401 (1965).
[12] L. Hung and E. A. Carter, Accurate simulations of metals at the mesoscale: Explicit treatment of 1 million atoms with quantum mechanics, Chem. Phys. Lett. **475**, 163 (2009).
[13] Y. A. Wang and E. A. Carter, *Orbital-free kinetic energy density functional theory* (Kluwer, 2000), Theoretical methods in condensed phase chemistry.
[14] N. Troullier and J. L. Martins, Efficient pseudopotentials for plane-wave calculations, Phys. Rev. B **43**, 1993 (1991).
[15] B. Zhou, Y. Alexander Wang, and E. A. Carter, Transferable local pseudopotentials derived via inversion of the Kohn-Sham equations in a bulk environment, Phys. Rev. B **69**, 125109 (2004).
[16] C. Huang and E. A. Carter, Transferable local pseudopotentials for magnesium, aluminum and silicon, Phys. Chem. Chem. Phys. **10**, 7109 (2008).
[17] J. Xia, C. Huang, I. Shin, and E. A. Carter, Can orbital-free density functional theory simulate molecules?, J. Chem. Phys. **136**, 084102 (2012).
[18] L.-W. Wang and M. P. Teter, Kinetic-energy functional of the electron density, Phys. Rev. B **45**, 13196 (1992).
[19] F. Perrot, Hydrogen-hydrogen interaction in an electron gas, J. Phys.: Condens. Matter **6**, 431 (1994).
[20] E. Smargiassi and P. A. Madden, Orbital-free kinetic-energy functionals for first-principles molecular dynamics, Phys. Rev. B **49**, 5220 (1994).
[21] Y. A. Wang, N. Govind, and E. A. Carter, Orbital-free kinetic-energy functionals for the nearly free electron gas, Phys. Rev. B **58**, 13465 (1998).
[22] Y. A. Wang, N. Govind, and E. A. Carter, Orbital-free kinetic-energy density functionals with a density-dependent kernel, Phys. Rev. B **60**, 16350 (1999).
[23] Y. A. Wang, N. Govind, and E. A. Carter, Erratum: Orbital-free kinetic-energy functionals for the nearly free electron gas [Phys. Rev. B **58**, 13465 (1998)], Phys. Rev. B **60**, 17162 (1999).
[24] Y. A. Wang, N. Govind, and E. A. Carter, Erratum: Orbital-free kinetic-energy density functionals with a density-dependent kernel [Phys. Rev. B **60**, 16350 (1999)], Phys. Rev. B **64**, 089903 (2001).
[25] G. S. Ho, C. Huang, and E. A. Carter, Describing metal surfaces and nanostructures with orbital-free density functional theory, Curr. Opin. Solid State Mater. Sci. **11**, 57 (2007).
[26] N. Choly, G. Lu, W. E, and E. Kaxiras, Multiscale simulations in simple metals: A density-functional-based methodology, Phys. Rev. B **71**, 094101 (2005).
[27] I. Shin, A. Ramasubramaniam, C. Huang, L. Hung, and E. A. Carter, Orbital-free density functional theory simulations of dislocations in aluminum, Philos. Mag. **89**, 3195 (2009).
[28] I. Shin and E. A. Carter, Possible origin of the discrepancy in Peierls stresses of fcc metals: First-principles simulations of dislocation mobility in aluminum, Phys. Rev. B **88**, 064106 (2013).

[29] I. Shin and E. A. Carter, Orbital-free density functional theory simulations of dislocations in magnesium, Modell. Simul. Mater. Sci. Eng. **20**, 015006 (2012).
[30] I. Shin and E. A. Carter, Simulations of dislocation mobility in magnesium from first principles, Int. J. Plast. **60**, 58 (2014).
[31] L. Hung and E. A. Carter, Ductile processes at aluminium crack tips: comparison of orbital-free density functional theory with classical potential predictions, Modell. Simul. Mater. Sci. Eng. **19**, 045002 (2011).
[32] X. Zhang and G. Lu, Calculation of fast pipe diffusion along a dislocation stacking fault ribbon, Phys. Rev. B **82**, 012101 (2010).
[33] G. Ho, M. T. Ong, K. J. Caspersen, and E. A. Carter, Energetics and kinetics of vacancy diffusion and aggregation in shocked aluminium via orbital-free density functional theory, Phys. Chem. Chem. Phys. **9**, 4951 (2007).
[34] A. Aguado, J. M. López, J. A. Alonso, and M. J. Stott, Melting in large sodium clusters: An orbital-free molecular dynamics study, J. Phys. Chem. B **105**, 2386 (2001).
[35] I. Shin and E. A. Carter, First-principles simulations of plasticity in body-centered-cubic magnesium–lithium alloys, Acta Mater. **64**, 198 (2014).
[36] K. M. Carling and E. A. Carter, Orbital-free density functional theory calculations of the properties of Al, Mg and Al–Mg crystalline phases, Modell. Simul. Mater. Sci. Eng. **11**, 339 (2003).
[37] S. Das, M. Iyer, and V. Gavini, Real-space formulation of orbital-free density functional theory using finite-element discretization: The case for Al, Mg, and Al-Mg intermetallics, Phys. Rev. B **92**, 014104 (2015).
[38] F. H. Allen, G. Bergerhoff, and I. Brown, *Crystallographic Databases* (International Union of Crystallography, Chester, 1987).
[39] http://www.whitehouse.gov/mgi.
[40] M. de Jong *et al.*, Charting the complete elastic properties of inorganic crystalline compounds, Scientific Data **2**, 150009 (2015).
[41] G. Kresse and J. Furthmüller, Efficient iterative schemes for ab initio total-energy calculations using a plane-wave basis set, Phys. Rev. B **54**, 11169 (1996).
[42] P. E. Blöchl, Projector augmented-wave method, Phys. Rev. B **50**, 17953 (1994).
[43] G. Kresse and D. Joubert, From ultrasoft pseudopotentials to the projector augmented-wave method, Phys. Rev. B **59**, 1758 (1999).
[44] J. P. Perdew, K. Burke, and M. Ernzerhof, Generalized gradient approximation made simple, Phys. Rev. Lett. **77**, 3865 (1996).
[45] H. J. Monkhorst and J. D. Pack, Special points for Brillouin-zone integrations, Phys. Rev. B **13**, 5188 (1976).
[46] M. Methfessel and A. T. Paxton, High-precision sampling for Brillouin-zone integration in metals, Phys. Rev. B **40**, 3616 (1989).
[47] M. Chen, J. Xia, C. Huang, J. M. Dieterich, L. Hung, I. Shin, and E. A. Carter, Introducing PROFESS 3.0: An advanced program for orbital-free density functional theory molecular dynamics simulations, Comput. Phys. Commun. **190**, 228 (2015).
[48] See Supplemental Material at [URL will be inserted by publisher] for more details on the phonon spectra of Mg and Al, derivation of elastic constants for Mg-Al Alloys, and the Voigt-Reuss-Hill approximation.
[49] B. Zhou, V. L. Ligneres, and E. A. Carter, Improving the orbital-free density functional theory description of covalent materials, J. Chem. Phys. **122**, 044103 (2005).

[50] J. Nocedal and S. Wright, *Numerical Optimization* (Springer, New York, 2006).
[51] L. Hung, C. Huang, and E. A. Carter, Preconditioners and electron density optimization in orbital-free density functional theory, Commun.Comput.Phys. **12**, 135 (2012).
[52] M. J. Mehl, B. M. Klein, and D. A. Papaconstantopoulos, in *Intermetallic Compounds*, edited by J. H. Westbrook, and R. L. Fleischer (John Wiley & Sons Ltd, 1994).
[53] S. Q. Wang and H. Q. Ye, *Ab initio* elastic constants for the lonsdaleite phases of C, Si and Ge, J. Phys.: Condens. Matter **15**, 5307 (2003).
[54] L. D. Landau, L. P. Pitaevskii, A. M. Kosevich, and E. M. Lifshitz, *Theory of Elasticity* (Butterworth-Heinemann, Oxford, 1986), 3rd edn.
[55] K. Parlinski, Z. Q. Li, and Y. Kawazoe, First-principles determination of the soft mode in cubic ZrO_2, Phys. Rev. Lett. **78**, 4063 (1997).
[56] A. Togo and I. Tanaka, First principles phonon calculations in materials science, Scripta Mater. **108**, 1 (2015).
[57] M. T. Dove, *Introduction to Lattice Dynamics* (Cambridge University Press, 2005).
[58] Z.-L. Liu, Phasego: A toolkit for automatic calculation and plot of phase diagram, Comput. Phys. Commun. **191**, 150 (2015).
[59] M. E. Straumanis, The precision determination of lattice constants by the powder and rotating crystal methods and applications, J. Appl. Phys **20**, 726 (1949).
[60] J. C. Crivello, T. Nobuki, and T. Kuji, Limits of the Mg–Al γ-phase range by ball-milling, Intermetallics **15**, 1432 (2007).
[61] N. Wang, W.-Y. Yu, B.-Y. Tang, L.-M. Peng, and W.-J. Ding, Structural and mechanical properties of $Mg_{17}Al_{12}$ and $Mg_{24}Y_5$ from first-principles calculations, J. Phys. D: Appl. Phys. **41**, 195408 (2008).
[62] T. Kazuhisa, Structural Analyses of the β and γ Alloys of Al-Mg, Jpn. J. Appl. Phys. **10**, 1311 (1971).
[63] C. Suryanarayana, S. K. Tiwari, and T. R. Anantharaman, A new metastable phase in the aluminium-magnesium system, Z. Metallkd. **69**, 155 (1978).
[64] A. Cooper, Precise lattice constants of germanium, aluminum, gallium arsenide, uranium, sulphur, quartz and sapphire, Acta Crystallogr. **15**, 578 (1962).
[65] J. Wang, J. Li, S. Yip, S. Phillpot, and D. Wolf, Mechanical instabilities of homogeneous crystals, Phys. Rev. B **52**, 12627 (1995).
[66] L. J. Slutsky and C. W. Garland, Elastic constants of magnesium from 4.2 K to 300 K, Phys. Rev. **107**, 972 (1957).
[67] Y. Le Page and P. Saxe, Symmetry-general least-squares extraction of elastic data for strained materials from *ab initio* calculations of stress, Phys. Rev. B **65**, 104104 (2002).
[68] G. Simmons and H. Wang, *Single Crystal Elastic Constants and Calculated Aggregate Properties. A Handbook* (The MIT Press, 1971), 2nd edn.
[69] M. Born, On the stability of crystal lattices. I, Math. Proc. Cambridge **36**, 160 (1940).
[70] J. Pokluda and P. Sandera, *Micromechanisms of Fracture and Fatigue: In a Multi-scale Context* (Springer; 2010 edition, 2010).
[71] F. Mouhat and F.-X. Coudert, Necessary and sufficient elastic stability conditions in various crystal systems, Phys. Rev. B **90**, 224104 (2014).

[72] S. F. Pugh, XCII. Relations between the elastic moduli and the plastic properties of polycrystalline pure metals, Philos. Mag. **45**, 823 (1954).
[73] L. Liu, H. Wang, G. Song, and J. N. Ye, Microstructure characteristics and mechanical properties of laser weld bonding of magnesium alloy to aluminum alloy, J. Mater. Sci. **42**, 565 (2006).
[74] G. Grimvall, B. Magyari-Köpe, V. Ozoliņš, and K. A. Persson, Lattice instabilities in metallic elements, Rev. Mod. Phys. **84**, 945 (2012).
[75] S. K. Mishra and S. S. Kushwaha, Model for the lattice dynamics of hexagonal-close-packed metals, Phys. Rev. B **18**, 6719 (1978).
[76] R. Stedman and G. Nilsson, Dispersion relations for phonons in aluminum at 80 and 300 K, Phys. Rev. **145**, 492 (1966).
[77] H. L. Su, M. Harmelin, P. Donnadieu, C. Baetzner, H. J. Seifert, H. L. Lukas, G. Effenberg, and F. Aldinger, Experimental investigation of the Mg-Al phase diagram from 47 to 63 at.% Al, J. Alloys Compd. **247**, 57 (1997).
[78] C. Suryanarayana and T. R. Anantharaman, On the structure of a metastable phase in the lead-bismuth system, Solid State Commun. **12**, 87 (1973).
[79] N. W. Ashcroft and N. D. Mermin, *Solid State Physics* (Brooks Cole, 1976).
[80] D. R. Lide, *CRC Handbook of Chemistry and Physics* (CRC Press, Boca Raton, Florida, 2003).
[81] A. Jain *et al.*, The materials project: A materials genome approach to accelerating materials innovation, APL Mater. **1**, 011002 (2013).